

Validating a Machine Learning Approach to Identify Quenched Jets in Heavy-Ion Collisions

Yilun Wu,^a Yi Chen,^a Julia Velkovska^a

^a *Vanderbilt University, Nashville, Tennessee, USA*

E-mail: yilun.wu@vanderbilt.edu, luna.chen@vanderbilt.edu,
julia.velkovska@vanderbilt.edu

ABSTRACT: Jet quenching is a phenomenon in heavy-ion collisions arising from jet interactions with the quark-gluon plasma (QGP). Its study is complicated by the interplay of multiple physics processes that affect jet observables. In addition, detector effects may influence the results and must be accounted for when identifying quenched jets. We employ a Long Short-Term Memory (LSTM) neural network trained on jet substructure, incorporating parton shower history, to predict jet-by-jet quenching levels. Using photon-jet samples from the JEWEL event generator, we show that the LSTM predictions strongly correlate with true jet energy loss. This validates that the model effectively learns the features of jet-QGP interaction. We simulate detector effects using DELPHES simulation framework and demonstrate that the method identifies quenching effects in a realistic environment. We test the approach with photon-jet momentum imbalance, jet fragmentation function, and jet shape, which were not included in the training, confirming its ability to distinguish true quenching features.

Contents

1	Introduction	1
2	Simulated samples	2
3	Jet reconstruction	4
3.1	Jet energy scale and resolution	4
4	Machine learning setup	7
5	Results	8
5.1	Training performance	8
5.2	Predictions for other observables	11
6	Conclusion	14

1 Introduction

Jets, collimated sprays of high- p_T hadrons produced from the fragmentation of hard-scattered partons, serve as excellent probes of the quark-gluon plasma (QGP) [1]. The phenomenon of jet quenching, first evidenced by the suppression of high- p_T hadrons at the Relativistic Heavy Ion Collider (RHIC) [2–6] and later confirmed at the Large Hadron Collider (LHC) [7–10], indicates the formation of QGP.

In heavy ion collisions, interactions with the QGP medium modify the total energy and the internal structure of the jets as compared to proton-proton collisions. Jet suppression [11–14] depends on factors such as jet flavor [15–17], path-length [18, 19] and fluctuations in medium density [20, 21]. To understand how lost energy is redistributed, studies have focused on jet-hadron correlations, such as jet shapes [22–24], and fragmentation functions [25, 26]. Beyond these, jet substructure measurements, including groomed jet observables [27–31] and energy-energy correlators [32], offer insights into jet evolution from parton showering to hadronization. Jet substructures are sensitive to the QGP resolution scale and color coherence [31], providing new perspectives on parton energy loss.

Disentangling these factors remains challenging. The experimental selections tend to have bias towards jets that lose less energy [33]. In addition, energy fluctuations from residual uncorrelated background particles [34, 35], detector resolution, and differences in the relative fraction of quark and gluon jets between heavy-ion and pp collisions [36, 37] may also appear as modifications. Knowing the jet energy loss on a jet-by-jet basis could greatly improve our understanding of jet-QGP interactions. In recent years, machine learning has proven to be effective in identifying individual jets based on their degrees of modification by the QGP [38–41], even when accounting for simplified thermal background [42, 43] and

detector smearing [44]. While most simulation-based studies achieve strong discrimination between jets from pp and PbPb collisions, it is a non-trivial task to cross-check whether classifiers distinguish true quenching features or over-learn from other effects that mimic quenching.

In this study, we train a Long Short-Term Memory (LSTM) network [45, 46] using supervised learning to distinguish quenched jets from vacuum jets on an individual basis. Our approach incorporates a realistic uncorrelated background along with the full detector response of both the calorimeter and the tracker. The resulting machine learning classifier employs the jet substructure and features of the parton shower history to preserve essential information about the parton energy loss in the QGP. We confirm that the quenching predictions from the LSTM strongly correlate with jet energy loss tagged by photons, even in the presence of underlying events and realistic detector responses. The trained classifier is then applied to observables not included in the training process as a cross-check to validate its ability to distinguish true quenching features from unrelated effects that mimic quenching.

The paper is organized as follows. In Section 2, we describe the event simulation procedure, as well as the detector response and correction methods. Section 3 discusses the jet reconstruction and energy correction process at the detector level. Section 4 details the supervised machine learning approach, including the input to it being optimized to capture jet energy loss information. In Section 5, we validate the quenching predictions of the trained classifier using various observables and identify medium jets with different levels of modification. In Section 6, we present our conclusions and outlook.

2 Simulated samples

Photon-jet samples are generated using JEWEL v2.2.0 [47, 48] with the "PPYJ" process at $\sqrt{s_{\text{NN}}} = 5.02$ TeV and a minimum transverse momentum of $\hat{p}_{\text{T}} = 40$ GeV. For heavy-ion jets, we enable the "simple" option with "recoil" on to include parton-medium interactions and medium response, while pp jets are simulated with the "vacuum" option.

Both medium and vacuum jet samples are embedded in a realistic heavy-ion background. The identical subtraction algorithm is used to prevent the neural network from learning uncorrelated background features that could mimic quenching effects [43]. The background simulation uses ANGANTYR [49] within PYTHIA 8.3 [50] for 0–10% central heavy-ion events at $\sqrt{s_{\text{NN}}} = 5.02$ TeV. The outgoing partons have a maximum transverse momentum of $\hat{p}_{\text{T}} = 5$ GeV¹. In Figure 1, the average momentum density for each simulated underlying event is correlated with the multiplicity and is found to be consistent with the CMS measurements [51]. The average momentum density obtained here is consistent with that reported in our previous study [52], but the present method has the advantage of capturing event-by-event fluctuations. More details of the uncorrelated underlying events are listed in Table 1.

We apply the machine learning approach to the photon-jet samples because the photon energy can be used to calibrate the jet energy loss independently. Similarly to what we would

¹For more information, see main42.cc and main42.cmnd in PYTHIA 8.3 examples.

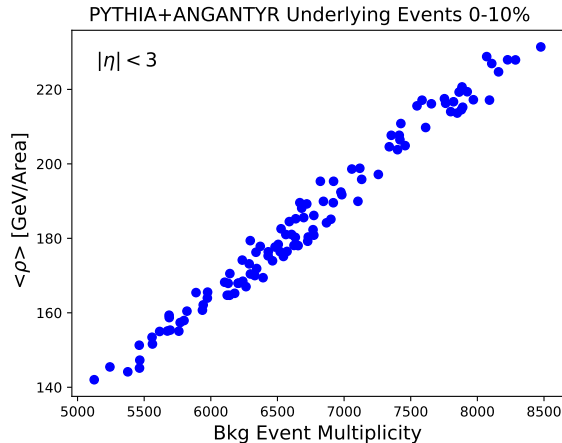


Figure 1: Scatter plot of average momentum density $\langle \rho \rangle$ and multiplicity for the underlying event simulated by ANGANTYR within PYTHIA 8.3.

Values	ANGANTYR
Pseudorapidity Interval	$ \eta < 3$
Mean Event Multiplicity	6727
Average Yield $\langle \frac{dN}{d\eta} \rangle$	1121
Average Transverse Momentum $\langle p_T \rangle$	1.05 GeV
Average Transverse Momentum Density $\langle \rho \rangle$	185.0 GeV/Area

Table 1: Parameters of the simulated underlying events.

do in experiments, we select JEWEL events where the highest- p_T photon and highest- p_T jet in the event have an angular separation of $7\pi/8$. The jets selected for training (learning set) have back-to-back photons with $p_T \in [200, 300]$ GeV, jet $p_T > 40$ GeV, and $|\eta| < 2.0$. This photon energy cut during training constrains the neural network, ensuring that it learns primarily from energy loss rather than fragmentation bias. However, a well-trained model applied to jet quenching classification across different observables (classification set) can adapt to a photon energy range without an upper limit (e.g., $p_T^\gamma > 200$ GeV).

The reconstructed jets are reclustered using the Cambridge/Aachen (C/A) algorithm [53] to extract jet substructure observables. The C/A algorithm organizes the jet constituents into an angularly ordered clustering tree. Within this structure, significant splittings are identified using the iterative soft-drop grooming procedure [54], which removes soft, wide-angle branches while retaining those that satisfy the soft-drop condition,

$$z_g \equiv \frac{\min(p_{T1}, p_{T2})}{p_{T1} + p_{T2}} > z_{\text{cut}} \left(\frac{\Delta R}{R_0} \right)^\beta, \quad (2.1)$$

where p_{T1} and p_{T2} are the transverse momenta of the two distinct subjet branches; ΔR

represents the angular separation between them and R_0 , set to 0.4, is the jet radius in this study. We set the parameters to $z_{\text{cut}} = 0.1$ and $\beta = 0$. Table 2 summarizes the cuts used in event selection.

Photon-Jet Selection	Learning set	Classification set
Centrality Interval	0-10%	0-10%
Jet Pseudorapidity Interval	$ \eta < 2.0$	$ \eta < 2.0$
Photon-Jet Angle Separation	$7\pi/8$	$7\pi/8$
Photon Energy	[200,300]GeV	>200 GeV
Jet Energy	>40 GeV	>100 GeV
Soft Drop Condition	$z_{\text{cut}} = 0.1, \beta = 0$	$z_{\text{cut}} = 0.1, \beta = 0$
No. Vac-Jets	38312	64074
No. Med-Jets	39629	74580

Table 2: Photon-jet selection cuts in training and classification.

To study detector effects on the reconstruction of substructure observables and neural network performance, we use DELPHES-3.5.0 [55] to simulate CMS detector conditions. The tracking efficiency of charged particles depends on η and ϕ , with a momentum threshold of 0.55 GeV. The particle energies are smeared according to the ECAL and HCAL calorimeter resolutions, matching those of the CMS detector. Additionally, we employ DELPHES particle-flow emulation, following the CMS approach [56], optimally combining information from all subdetectors to reconstruct and identify individual particles.

3 Jet reconstruction

Jets are reconstructed using the anti- k_T algorithm [57] from the emulated particle-flow candidates with a distance parameter of $R = 0.4$. The underlying event particles are subtracted using the event-wide constituent subtraction method [58]. The maximum distance parameter between the signal and the background particles is set to $\Delta R_{\text{max}} = 0.3$, with a p_T weight of $\alpha = 1$.

3.1 Jet energy scale and resolution

The reconstructed jets are matched to their GEN-level counterparts to determine the relative energy scales. Figures 2 and 3 illustrate the jet energy scale (JES) for reconstructed medium and vacuum jets in simulated PbPb and pp collisions, respectively, with detector responses simulated by DELPHES, compared to jets at GEN-level. The calibration of the jet energy recovers the jet energy from the RECO level to the GEN level as a function of p_T , η , and ϕ . Figure 4 shows the jet energy resolution (JER) for JEWEL-Med (PbPb) and JEWEL-Vac (pp) jets.

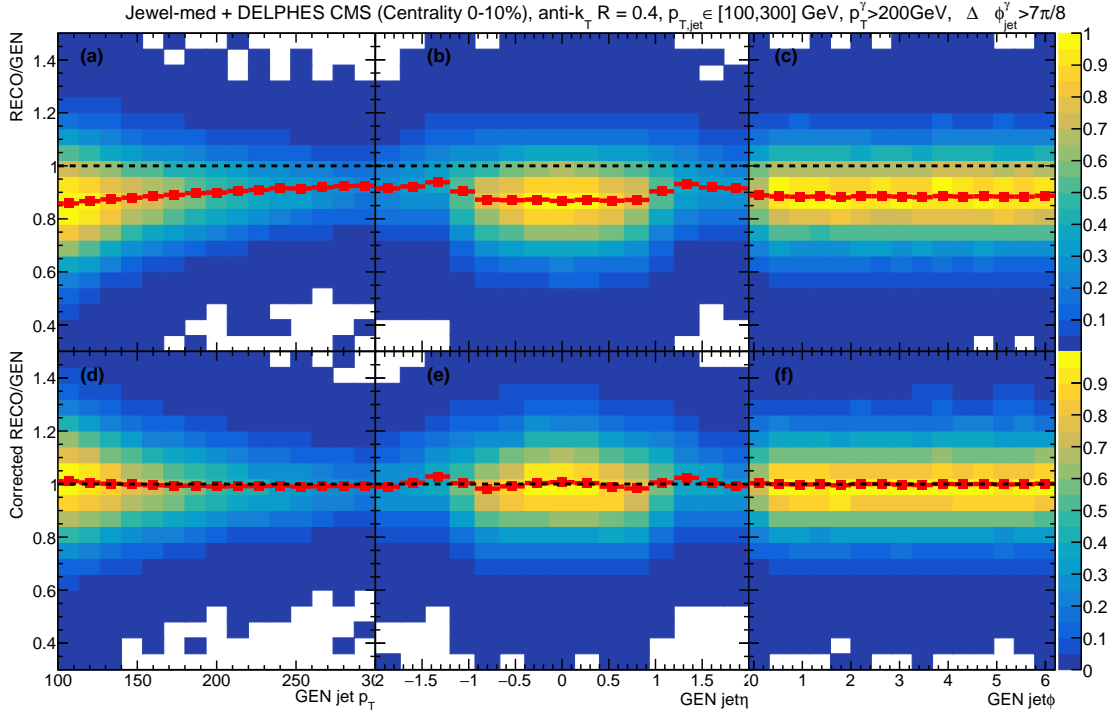


Figure 2: JES of reconstructed JEWEL-Med (PbPb) jets from DELPHES Energy Flow candidates. The upper panel shows JES before jet energy calibration, while the lower panel shows JES after calibration. (a–c) JES as a function of jet p_T , η , and ϕ , respectively. (d–f) Corresponding distributions after jet energy corrections.

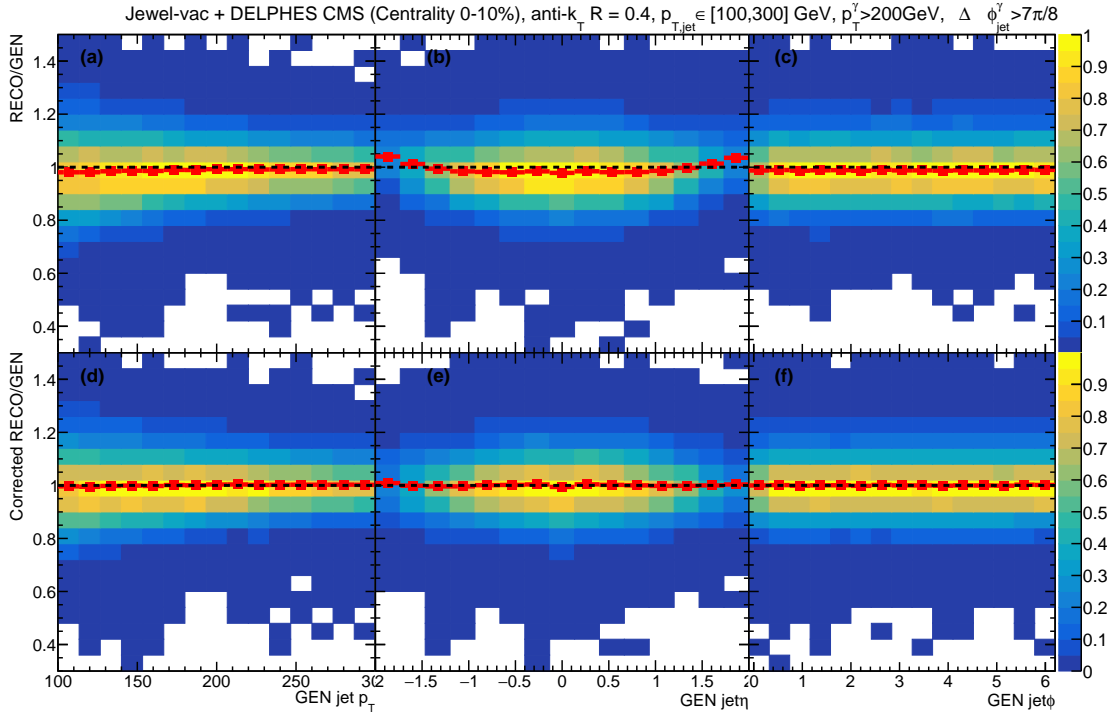


Figure 3: JES of reconstructed JEWEL-Vac (pp) jets from DELPHES Energy Flow candidates. The upper panel shows JES before jet energy calibration, while the lower panel shows JES after calibration. (a–c) JES as a function of jet p_T , η , and ϕ , respectively. (d–f) Corresponding distributions after jet energy corrections.

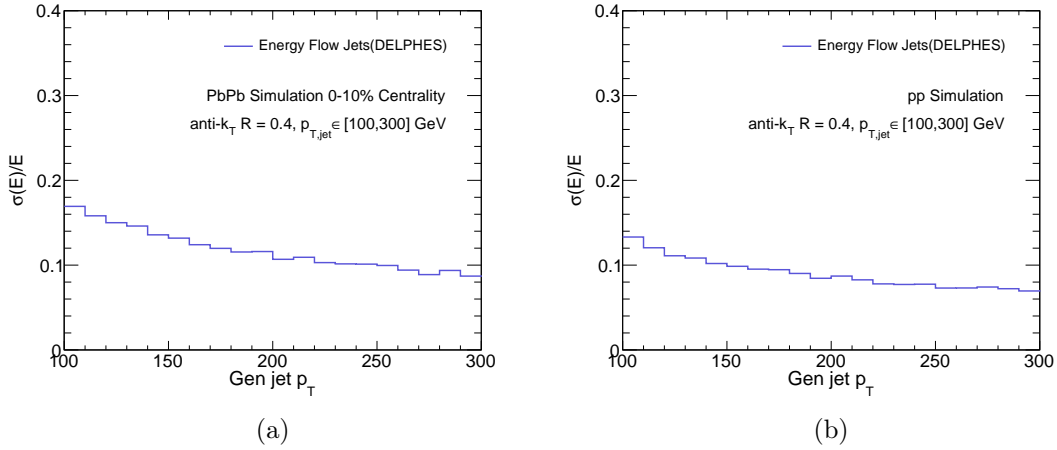


Figure 4: JER of reconstructed medium/vacuum jets from DELPHES Energy Flow candidates. (a): JER for medium jets; (b): JER for vacuum jets.

4 Machine learning setup

Jets are declustered following angular-ordered structures (Sec. 3), retaining the harder subjet as sequential input for machine learning. Each selected splitting is represented by a feature vector x_t , comprising the momentum fraction z , the angular distance ΔR , the perpendicular momentum k_\perp and the invariant mass m_{inv} , derived from the declustered subjet pair:

$$\begin{aligned}
 z &= \frac{\min(p_{T,i}, p_{T,j})}{p_{T,i} + p_{T,j}}, \\
 \Delta R &= \sqrt{(\phi_i - \phi_j)^2 + (\eta_i - \eta_j)^2}, \\
 k_\perp &= \min(p_{T,i}, p_{T,j}) * \Delta R, \\
 m_{\text{inv}} &= \sqrt{(E_i + E_j)^2 - (\mathbf{p}_i + \mathbf{p}_j)^2}, \\
 x_t &= [z, \Delta R, k_\perp, m_{\text{inv}}],
 \end{aligned}
 \tag{4.1}$$

where i, j denote the subjets in the declustering step t . In this way, sequential vectors $[x_0, \dots, x_t, \dots]$ are extracted and used in the training of a neural network. Sequential vectors, which encode the showering history of the jet while preserving modifications from QGP medium, serve as input to train a neural network composed of LSTM and fully connected (FC) layers implemented in PyTorch [59]. As a type of recurrent neural network, an LSTM is particularly suited to learn from sequential data, using internal "gates" [46] to selectively retain or discard information over time steps. This allows it to effectively capture the patterns of jet-QGP interaction.

Jet quenching identification is framed as a classification problem of supervised learning, with vacuum jets labeled 0 and medium jets labeled 1. In the final step, predicted values for all input jets are used to compute batch losses via the weighted mean squared error (MSE) loss function:

$$l_{\text{MSE}} = \frac{\sum_{\text{batch}} \omega_i * (x_i - y_i)^2}{\sum_{\text{batch}} \omega_i},
 \tag{4.2}$$

where x_i and y_i denote the predicted and true labels of the i th jet, respectively, while ω_i Model hyper-parameters, including the number of LSTM layers, fully connected (FC) layer dimensions¹, epochs, batch size, learning rate, and decay factor, are optimized using the Hyperopt package [60]. Following the same training method as in [42], we perform 50 search iterations, training each configuration three times, and select the model with the lowest validation loss as the best-performing. The corresponding optimal hyper-parameters are listed in Table 3.

¹The input dimension of the first FC layer equals the LSTM hidden size.

Parameters	GEN Level	RECO Level
No. of LSTM Layers	2	2
FC Dim 1	14	14
FC Dim 2	8	4
No. of Epochs	50	50
Batch Size	12000	10000
Learning Rate	0.04754	0.0416
Decay Factor	0.9728	0.9810

Table 3: List of hyper-parameters related to the neural network architecture and the training process, and their optimal values after hyper-tuning.

5 Results

5.1 Training performance

The trained neural network can be used as a classifier to predict the probability that a jet is quenched. Figure 5 presents the distributions of the LSTM output and the receiver operating characteristic (ROC) curve. During training, the unquenched jets are labeled as 0, while the quenched jets are labeled as 1. The probability metric for jet quenching, learned during training, produces an output between 0 and 1 for each class.

Samples from the quenched class (JEWEL-Med) are divided into two subsets: the top 40% and the bottom 60%, based on the LSTM output. To explore the relationship between LSTM output and quenching effects, we present the distributions of groomed jet substructure variables in Fig. 6 for both subsets separately. For comparison, samples from the unquenched class (JEWEL-Vac), serving as a baseline, are also included.

The two subsets exhibit different levels of quenching effects. The top 40% of the quenched class shows significant jet substructure modifications, with enhanced wider and softer splittings. In contrast, the bottom 60% exhibits a quenching pattern more similar to the unquenched class. Neural networks trained at both the GEN and RECO levels yield consistent trends, indicating that despite detector smearing, the network effectively quantifies quenching effects. This shows that the machine learning approach successfully accounts for the detector effects on the inputs.

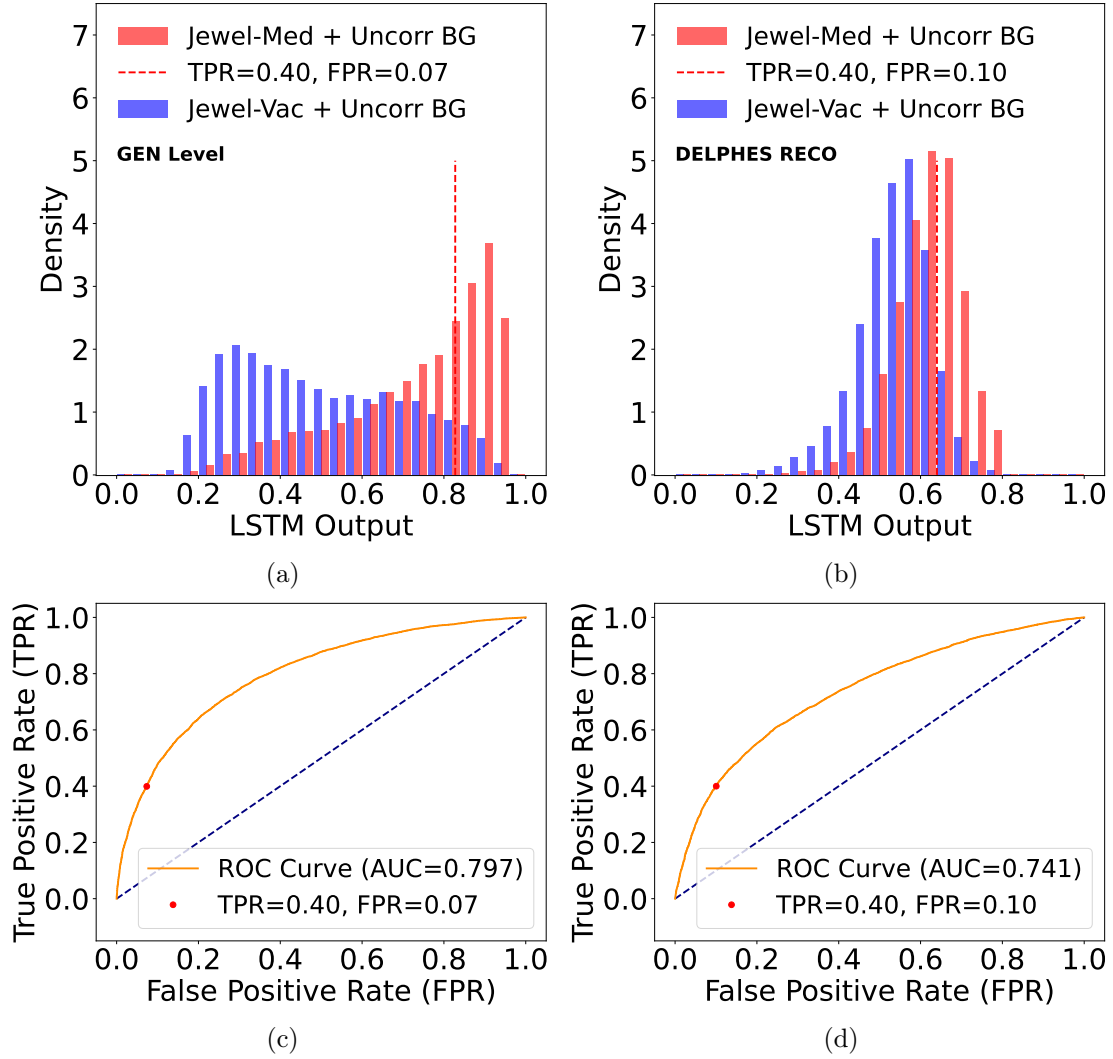


Figure 5: Binary classification performance of the LSTM neural network at the GEN level (left) and RECO level (right). (a, b) Classification output; (c, d) ROC curve.

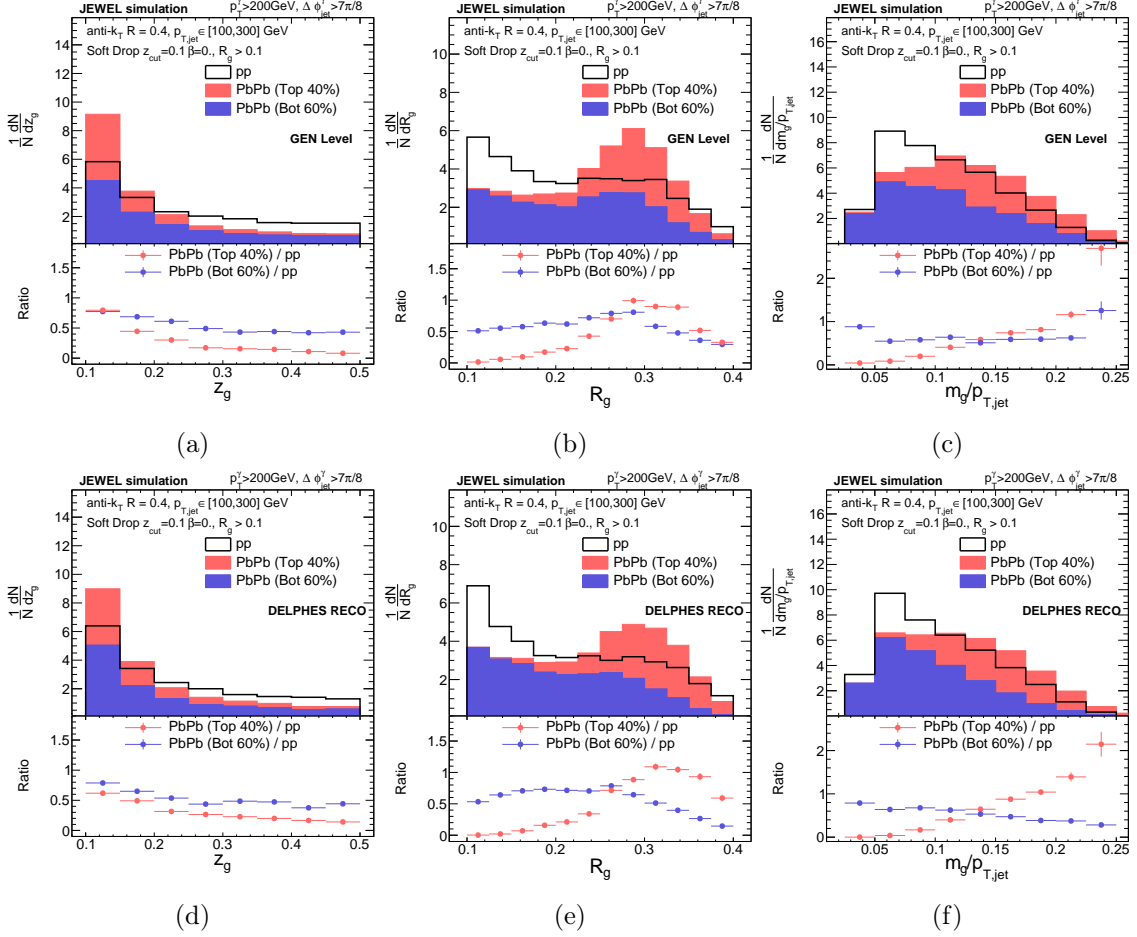


Figure 6: Neural network trained on GEN level (upper panels) and RECO level (lower panels) substructure variables of groomed jets, classifying quenched jets into two categories: top 40% medium-like jets and bottom 60% vacuum-like jets. (a, d) Momentum fraction (splitting function); (b, e) angular separation; (c, f) invariant jet mass.

5.2 Predictions for other observables

To better understand the relationship between the ML classifier results and the quenching effects, we apply the LSTM output to observables that were not included in the training. To study the quenching effects in detail, we assign a "quenching level" to each jet from 0 to 100%, with 0% being the most quenched, based on the LSTM output. The quenched sample is divided into five subsets equally. The most quenched class is denoted by Q 0-20%, while the least quenched class is denoted by Q 80-100%.

Photon-jet momentum imbalance: For the five quenching classes, we measure the distributions of the photon-jet energy fraction at the GEN level in Fig. 7a and at the RECO level in Fig. 7b. With or without detector effects, the most quenched class (Q 0-20%) exhibits the greatest transverse momentum imbalance between the back-to-back jet and the photon. As the quenching level decreases toward the least quenched class (Q 80-100%), the transverse momentum between the jet and the photon becomes more balanced, with the ratio distribution shifting closer to zero (no energy loss). The ordering in the peak positions of the five quenching classes remains consistent when the detector effects are included.

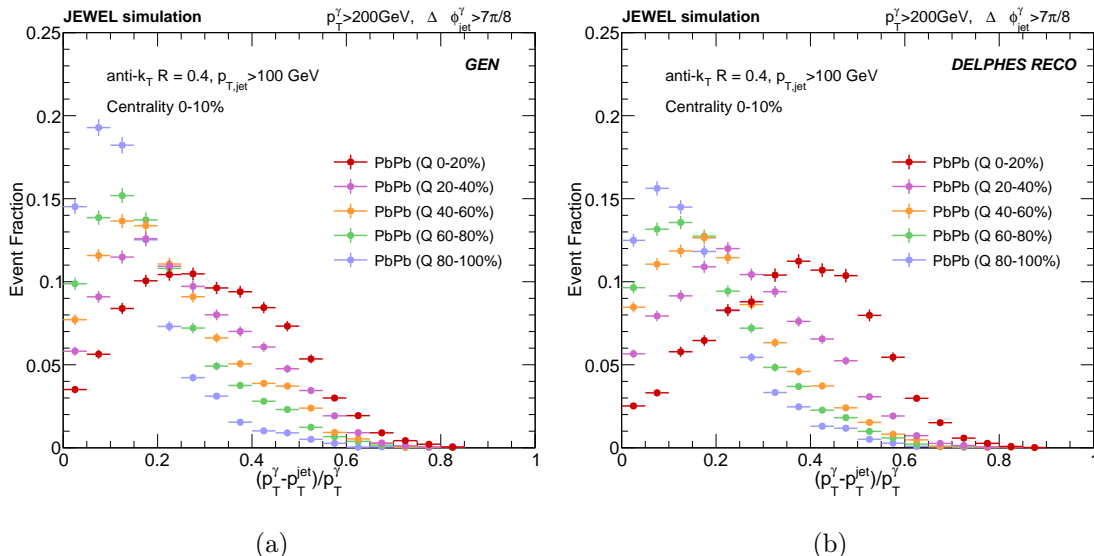


Figure 7: Photon-jet momentum imbalance of five quenching classes from JEWEL-Med (PbPb) identified by the LSTM classifier. (a) Five classes with different modifications compared to inclusive pp jets at the GEN level. (b) RECO level with detector effects simulated using DELPHES.

Jet fragmentation function: The LSTM output is also applied to the jet fragmentation function,

$$z = \frac{p_{||}^{\text{track}}}{p^{\text{jet}}}, \xi = \ln\left(\frac{1}{z}\right), \quad (5.1)$$

as shown in Fig. 8. At both the GEN level (Fig. 8a) and the RECO level (Fig. 8b), as the predicted quenching level increases, the jets exhibit greater enhancement in the large ξ

region, indicating that more soft particles enter the jet cone. Meanwhile, ML-identified high-quenched jets (Q 0–20%) show a greater depletion in the intermediate ξ region compared to weakly quenched jets (Q 80–100%), indicating increased energy loss. The jet fragmentation functions exhibit varying degrees of modification relative to the baseline, represented by the ratio of inclusive JEWEL-Med jets to inclusive JEWEL-Vac jets, categorized according to their ML-determined quenching levels. The RECO level results recover the GEN level ones with tracking efficiency corrected.

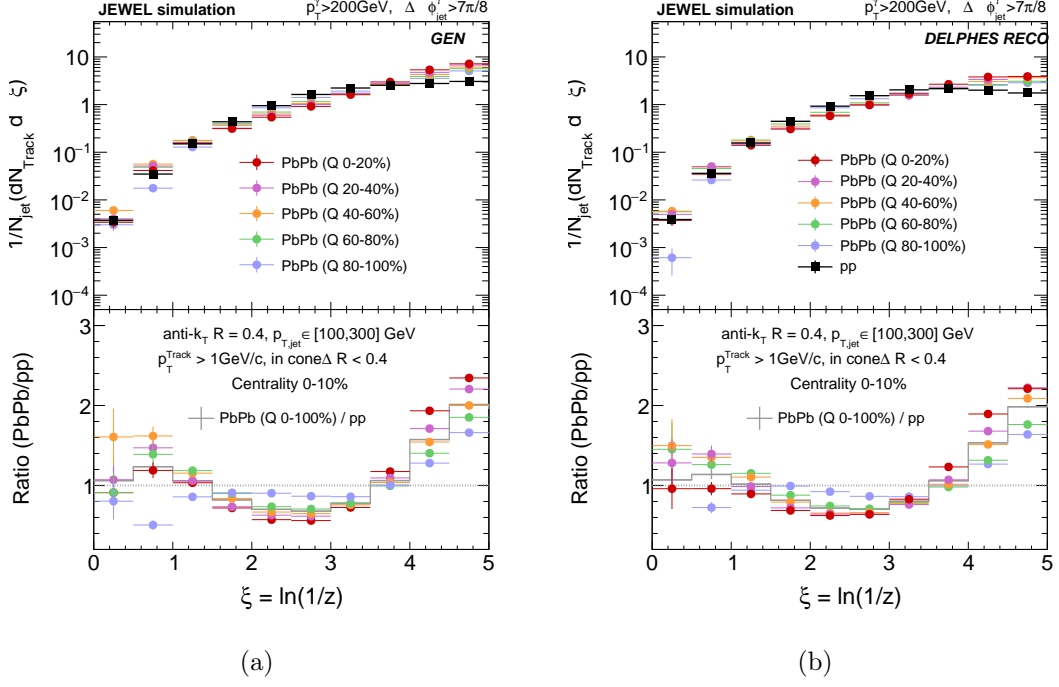


Figure 8: Jet fragmentation function of five classes identified by the LSTM classifier. (a) Five classes of JEWEL-Med (PbPb) jets, showing different modifications compared to inclusive pp jets at the GEN level. (b) RECO level with detector effects simulated using DELPHES.

Jet momentum profile: ML classification results for the jet momentum profile (integrated jet shape),

$$P(r) = \frac{1}{\delta r} \frac{1}{N_{\text{jet}}} \sum_{\text{jets}} \sum_{\text{tracks} \in [r_a, r_b]} p_T^{\text{track}} \quad (5.2)$$

are shown in Fig. 9. At both the GEN level (Fig. 9a) and the RECO level (Fig. 9b), the jets exhibit greater enhancement in the larger ΔR and greater depletion in the smaller ΔR as the predicted quenching level increases. This modification trend is consistent with the scenario in which strongly quenched jets exhibit a greater redistribution of jet energy to softer particles, extending to large angles away from the jet axis. Meanwhile, the least quenched jets (Q 80–100%) predicted by the neural network behave like vacuum jets, with their ratios to inclusive pp jets following a flatter trend compared to other quenched classes.

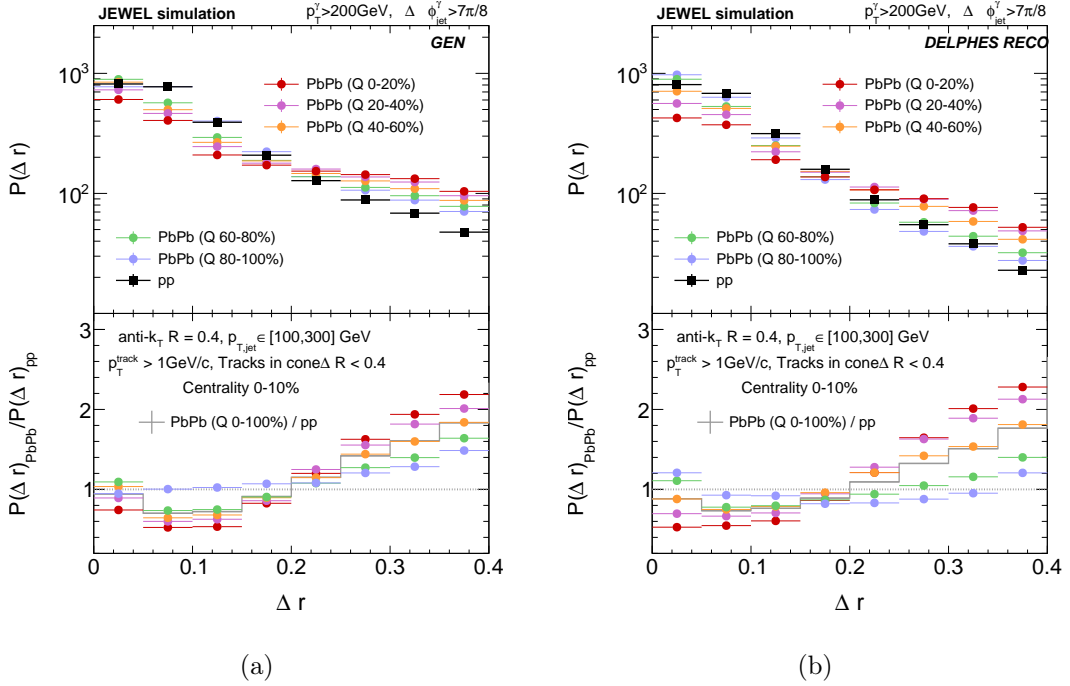


Figure 9: Jet momentum profile of five classes with different quenching levels identified by the LSTM neural network. (a) Five quenching classes for the JEWEL-Med (PbPb) jet sample at the GEN level. (b) RECO level with detector effects simulated using DELPHES.

6 Conclusion

We demonstrated that a well-trained ML classifier based on sequential jet substructures can effectively distinguish true quenching features from other sources that may mimic quenching, such as thermal background and detector effects. To validate this, we cross-checked observables not included in the training process, e.g. photon-jet momentum imbalance, jet fragmentation function, and jet momentum profile. We found that the jets identified by the ML classifier with varying quenching levels exhibit the corresponding modifications in these observables.

Using the DELPHES simulation of the CMS detector response and particle flow candidate equivalents, we predicted the results of applying the ML method to data analysis. The results indicated that, even with detector effects, our ML classifier can still effectively learn from quenching features, consistent with the jet energy loss estimated from the photon energy. We demonstrated significant potential of the machine learning approach for application to experimental data, where it can analyze a wide range of jet observables on a jet-by-jet basis. Such studies will help disentangle a variety of competing mechanisms that lead to jet modifications in QGP.

Acknowledgments

The authors thank R. Kunnawalkam Elayavalli and J. Viinikainen for insightful discussions. The authors also acknowledge the support of the Vanderbilt ACCRE computing facility. This work was supported by US Department of Energy Grant No. DE-FG05-92ER40712.

References

- [1] J. D. Bjorken, *Energy Loss of Energetic Partons in Quark - Gluon Plasma: Possible Extinction of High $p(t)$ Jets in Hadron - Hadron Collisions*, .
- [2] PHENIX Collaboration, *Suppression of hadrons with large transverse momentum in central Au+Au collisions at $\sqrt{s_{NN}} = 130$ GeV*, *Phys. Rev. Lett.* **88** (2002) 022301, [[nucl-ex/0109003](#)].
- [3] STAR Collaboration, *Centrality dependence of high p_T hadron suppression in Au+Au collisions at $\sqrt{s_{NN}} = 130$ -GeV*, *Phys. Rev. Lett.* **89** (2002) 202301, [[nucl-ex/0206011](#)].
- [4] PHENIX Collaboration, *Suppressed π^0 production at large transverse momentum in central Au+Au collisions at $\sqrt{s_{NN}} = 200$ GeV*, *Phys. Rev. Lett.* **91** (2003) 072301, [[nucl-ex/0304022](#)].
- [5] STAR Collaboration, *Transverse momentum and collision energy dependence of high p_T hadron suppression in Au+Au collisions at ultrarelativistic energies*, *Phys. Rev. Lett.* **91** (2003) 172302, [[nucl-ex/0305015](#)].
- [6] STAR Collaboration, *Disappearance of back-to-back high p_T hadron correlations in central Au+Au collisions at $\sqrt{s_{NN}} = 200$ -GeV*, *Phys. Rev. Lett.* **90** (2003) 082302, [[nucl-ex/0210033](#)].
- [7] ALICE Collaboration, *Suppression of charged particle production at large transverse momentum in central Pb-Pb collisions at $\sqrt{s_{NN}} = 2.76$ TeV*, *Phys. Lett. B* **696** (2011) 30, [[1012.1004](#)].
- [8] ALICE Collaboration, *Particle-yield modification in jetlike azimuthal dihadron correlations in Pb-Pb collisions at $\sqrt{s_{NN}} = 2.76$ TeV*, *Phys. Rev. Lett.* **108** (2012) 092301, [[1110.0121](#)].
- [9] CMS Collaboration, *Study of high- p_T charged particle suppression in PbPb compared to pp collisions at $\sqrt{s_{NN}} = 2.76$ TeV*, *Eur. Phys. J. C* **72** (2012) 1945, [[1202.2554](#)].
- [10] ATLAS Collaboration, *Measurement of charged-particle spectra in Pb+Pb collisions at $\sqrt{s_{NN}} = 2.76$ TeV with the ATLAS detector at the LHC*, *JHEP* **09** (2015) 050, [[1504.04337](#)].
- [11] CMS Collaboration, *Study of high-pt charged particle suppression in pbbp compared to pp collisions at $\sqrt{s_{NN}} = 2.76$ TeV*, *The European Physical Journal C* **72** (2012) , [[1202.2554](#)].
- [12] ATLAS Collaboration, *Measurement of the jet radius and transverse momentum dependence of inclusive jet suppression in lead-lead collisions at $\sqrt{s_{NN}} = 2.76$ TeV with the ATLAS detector*, *Phys. Lett. B* **719** (2013) 220, [[1208.1967](#)].
- [13] ALICE Collaboration, *Measurement of charged jet suppression in Pb-Pb collisions at $\sqrt{s_{NN}} = 2.76$ TeV*, *JHEP* **03** (2014) 013, [[1311.0633](#)].
- [14] ALICE Collaboration, *Measurement of jet suppression in central Pb-Pb collisions at $\sqrt{s_{NN}} = 2.76$ TeV*, *Phys. Lett. B* **746** (2015) 1, [[1502.01689](#)].
- [15] CMS Collaboration, *Evidence of b-Jet Quenching in PbPb Collisions at $\sqrt{s_{NN}} = 2.76$ TeV*, *Phys. Rev. Lett.* **113** (2014) 132301, [[1312.4198](#)].
- [16] ATLAS Collaboration, *Comparison of inclusive and photon-tagged jet suppression in 5.02 TeV Pb+Pb collisions with ATLAS*, *Phys. Lett. B* **846** (2023) 138154, [[2303.10090](#)].
- [17] ATLAS Collaboration, *Measurement of the nuclear modification factor of b-jets in 5.02 TeV Pb+Pb collisions with the ATLAS detector*, *Eur. Phys. J. C* **72** **83** (2023) , [[2204.13530](#)].

- [18] ATLAS Collaboration, *Measurements of azimuthal anisotropies of jet production in Pb + Pb collisions at $\sqrt{s_{NN}} = 5.02$ TeV with the ATLAS detector*, *Phys. Rev. C* **105** (2022) 064903, [2111.06606].
- [19] CMS Collaboration, *Azimuthal anisotropy of dijet events in PbPb collisions at $\sqrt{s_{NN}} = 5.02$ TeV*, *JHEP* **2023** (2023) , [2210.08325v2].
- [20] J. Noronha-Hostler, B. Betz, M. Gyulassy, M. Luzum, J. Noronha, I. Portillo et al., *Cumulants and nonlinear response of high p_T harmonic flow at $\sqrt{s_{NN}} = 5.02$ TeV*, *Phys. Rev. C* **95** (2017) 044901, [1609.05171v2].
- [21] A. Holtermann, J. Noronha-Hostler, A. M. Sickles and X. Wang, *Multiparticle correlations, cumulants, and moments sensitive to fluctuations in rare-probe azimuthal anisotropy in heavy ion collisions*, *Phys. Rev. C* **108** (2023) 064901, [2307.16796v2].
- [22] CMS Collaboration, *Modification of jet shapes in PbPb collisions at $\sqrt{s_{NN}} = 2.76$ TeV*, *Phys. Lett. B* **730** (2014) 243, [1310.0878].
- [23] ALICE Collaboration, *Measurement of jet radial profiles in Pb-Pb collisions at $\sqrt{s_{NN}} = 2.76$ TeV*, *Phys. Lett. B* **796** (2019) 204–219, [1904.13118].
- [24] ATLAS Collaboration, *Measurement of angular and momentum distributions of charged particles within and around jets in Pb+Pb and pp collisions at $\sqrt{s_{NN}} = 5.02$ TeV with the ATLAS detector*, *Phys. Rev. C* **100** (2019) 064901, [1908.05264].
- [25] CMS Collaboration, *Measurement of jet fragmentation in PbPb and pp collisions at $\sqrt{s_{NN}} = 2.76$ TeV*, *Phys. Rev. C* **90** (2014) 024908, [1406.0932].
- [26] ATLAS Collaboration, *Measurement of jet fragmentation in Pb+Pb and pp collisions at $\sqrt{s_{NN}} = 2.76$ TeV with the ATLAS detector at the LHC*, *Eur. Phys. J. C* **77** (2017) 379, [1702.00674].
- [27] CMS Collaboration, *Measurement of the Splitting Function in pp and Pb-Pb Collisions at $\sqrt{s_{NN}} = 5.02$ TeV*, *Phys. Rev. Lett.* **120** (2018) 142302, [1708.09429].
- [28] STAR Collaboration, *Differential measurements of jet substructure and partonic energy loss in Au+Au collisions at $\sqrt{s_{NN}} = 200$ GeV*, *Phys. Rev. C* **105** (2022) 044906, [2109.09793].
- [29] ALICE Collaboration, *Measurement of the groomed jet radius and momentum splitting fraction in pp and Pb–Pb collisions at $\sqrt{s_{NN}} = 5.02$ TeV*, *Phys. Rev. Lett.* **128** (2022) 102001, [2107.12984].
- [30] CMS Collaboration, *Measurement of the groomed jet mass in PbPb and pp collisions at $\sqrt{s_{NN}} = 5.02$ TeV*, *JHEP* **2018** (2018) , [1805.05145].
- [31] ATLAS Collaboration, *Measurement of substructure-dependent jet suppression in Pb + Pb collisions at 5.02 TeV with the ATLAS detector*, *Phys. Rev. C* **107** (2023) 054909, [2211.11470v2].
- [32] CMS Collaboration, *Energy-energy correlators from PbPb and pp collisions at 5.02 TeV*, 2024, <https://cds.cern.ch/record/2906425/files/HIN-23-004-pas.pdf>.
- [33] CMS Collaboration, *Girth and groomed radius of jets recoiling against isolated photons in lead-lead and proton-proton collisions at $\sqrt{s_{NN}} = 5.02$ tev*, *Physics Letters B* **861** (2025) 139088, [2405.02737].
- [34] M. Connors, C. Nattrass, R. Reed and S. Salur, *Jet measurements in heavy ion physics*, *Reviews of Modern Physics* **90** (2018) , [1705.01974v2].

- [35] J. Mulligan and M. Ploskon, *Identifying groomed jet splittings in heavy-ion collisions*, *Phys. Rev. C* **102** (2020) 044913, [[2006.01812](#)].
- [36] F. Ringer, B.-W. Xiao and F. Yuan, *Can we observe jet P -broadening in heavy-ion collisions at the LHC?*, *Phys. Lett. B* **808** (Sept., 2020) 135634, [[1907.12541](#)].
- [37] L. Apolinário, R. K. Elayavalli, N. O. Madureira, J.-X. Sheng, X.-N. Wang and Z. Yang, *Flavor dependence of Energy-energy correlators*, [2502.11406](#).
- [38] L. Apolinário, N. F. Castro, M. Crispim Romão, J. G. Milhano, R. Pedro and F. C. R. Peres, *Deep Learning for the classification of quenched jets*, *JHEP* **11** (2021) 219, [[2106.08869](#)].
- [39] Y.-L. Du, D. Pablos and K. Tywoniuk, *Deep learning jet modifications in heavy-ion collisions*, *JHEP* **21** (2020) 206, [[2012.07797](#)].
- [40] Y. S. Lai, J. Mulligan, M. Płoskoń and F. Ringer, *The information content of jet quenching and machine learning assisted observable design*, *JHEP* **2022** (2022) 11, [[2111.14589](#)].
- [41] M. Crispim Romão, J. Guilherme Milhano and M. van Leeuwen, *Jet substructure observables for jet quenching in quark gluon plasma: A machine learning driven analysis*, *SciPost Physics* **16** (2024) , [[2304.07196v2](#)].
- [42] L. Liu, J. Velkovska, Y. Wu and M. Verweij, *Identifying quenched jets in heavy ion collisions with machine learning*, *JHEP* **2023** (2023) .
- [43] J. a. A. Gonçalves and J. G. Milhano, *Apples to Apples in Jet Quenching: robustness of Machine Learning classification of quenched jets to Underlying Event contamination*, [2501.14015](#).
- [44] U. S. Qureshi and R. K. Elayavalli, *Model-agnostic tagging of quenched jets in heavy-ion collisions*, [2411.19389](#).
- [45] S. Hochreiter and J. Schmidhuber, *Long short-term memory*, *Neural computation* **9** (1997) 1735–1780.
- [46] A. Sherstinsky, *Fundamentals of recurrent neural network (rnn) and long short-term memory (lstm) network*, *Physica D: Nonlinear Phenomena* **404** (2020) 132306.
- [47] K. C. Zapp, F. Krauss and U. A. Wiedemann, *A perturbative framework for jet quenching*, *JHEP* **03** (2013) 080, [[1212.1599](#)].
- [48] R. Kunnawalkam Elayavalli and K. C. Zapp, *Medium response in JEWEL and its impact on jet shape observables in heavy ion collisions*, *JHEP* **07** (2017) 141, [[1707.01539](#)].
- [49] C. Bierlich, G. Gustafson, L. Lönnblad and H. Shah, *The angantyr model for heavy-ion collisions in pythia8*, *JHEP* **2018** (2018) , [[1806.10820v2](#)].
- [50] C. Bierlich, S. Chakraborty, N. Desai, L. Gellersen, I. Helenius, P. Ilten et al., *A comprehensive guide to the physics and usage of PYTHIA 8.3*, *SciPost Phys. Codebases* (2022) 8, [[2203.11601v1](#)].
- [51] CMS Collaboration, *Overview of high-density QCD studies with the CMS experiment at the LHC*, [2405.10785](#).
- [52] L. Liu, *Github repository for jet quenching studies with machine learning*, 2022.
- [53] Y. L. Dokshitzer, G. D. Leder, S. Moretti and B. R. Webber, *Better jet clustering algorithms*, *JHEP* **08** (1997) 001, [[hep-ph/9707323](#)].

- [54] A. J. Larkoski, S. Marzani, G. Soyez and J. Thaler, *Soft drop*, *JHEP* **05** (2014) 146, [[1402.2657](#)].
- [55] J. de Favereau, C. Delaere, P. Demin, A. Giammanco, V. Lemaître, A. Mertens et al., *Delphes 3: a modular framework for fast simulation of a generic collider experiment*, *JHEP* **2014** (2014) , [[1307.6346v3](#)].
- [56] CMS Collaboration, *Particle-Flow Event Reconstruction in CMS and Performance for Jets, Taus, and MET*, tech. rep., CERN, Geneva, 2009.
- [57] M. Cacciari, G. P. Salam and G. Soyez, *The anti- k_t jet clustering algorithm*, *JHEP* **04** (2008) 063, [[0802.1189](#)].
- [58] P. Berta, M. Spousta, D. W. Miller and R. Leitner, *Particle-level pileup subtraction for jets and jet shapes*, *JHEP* **06** (2014) 092, [[1403.3108](#)].
- [59] A. Paszke, S. Gross, F. Massa, A. Lerer, J. Bradbury, G. Chanan et al., *Pytorch: An imperative style, high-performance deep learning library*, in *Advances in Neural Information Processing Systems 32* (H. Wallach, H. Larochelle, A. Beygelzimer, F. d'Alché-Buc, E. Fox and R. Garnett, eds.), pp. 8024–8035. Curran Associates, Inc., 2019.
- [60] J. Bergstra, D. Yamins and D. Cox, *Making a science of model search: Hyperparameter optimization in hundreds of dimensions for vision architectures*, in *Proceedings of the 30th International Conference on Machine Learning* (S. Dasgupta and D. McAllester, eds.), vol. 28 of *Proceedings of Machine Learning Research*, (Atlanta, Georgia, USA), pp. 115–123, PMLR, 17–19 Jun, 2013, <https://proceedings.mlr.press/v28/bergstra13.html>.